





Article

# The Effect of Equal-Channel Angular Pressing on Microstructure, Mechanical Properties, and Biodegradation Behavior of Magnesium Alloyed with Silver and Gadolinium

Boris Straumal <sup>1,2,3,11,\*</sup>, Natalia Martynenko <sup>1,4</sup>, Diana Temralieva <sup>1,4</sup>, Vladimir Serebryany <sup>4</sup>, Natalia Tabachkova <sup>1,5</sup> , Igor Shchetinin <sup>1</sup>, Natalia Anisimova <sup>1,6</sup> , Mikhail Kiselevskiy <sup>1,6</sup>, Alexandra Kolyanova <sup>4</sup>, Georgy Raab <sup>7</sup>, Regine Willumeit-Römer <sup>8</sup> , Sergey Dobatkin <sup>1,4</sup> and Yuri Estrin <sup>9,10</sup> 

<sup>1</sup> National University of Science and Technology “MISIS”, Leninsky Avenue 4, 119991 Moscow, Russia; nata\_roug@mail.ru (N.M.); diana4-64@mail.ru (D.T.); ntabachkova@gmail.com (N.T.); ingvvar@gmail.com (I.S.); n\_anisimova@list.ru (N.A.); kisele@inbox.ru (M.K.); dobatkin.sergey@gmail.com (S.D.)

<sup>2</sup> Institute of Solid State Physics and Chernogolovka Scientific Center of the Russian Academy of Sciences, Chernogolovka, Leninskiy Prospekt, 14, 119991 Moscow, Russia

<sup>3</sup> Institute of Nanotechnology, Karlsruhe Institute of Technology, Eggenstein-Leopoldshafen, 76131 Karlsruhe, Germany

<sup>4</sup> A.A. Baikov Institute of Metallurgy and Materials Science of the RAS, Leninskiy Prospekt, 49, 119334 Moscow, Russia; vns@imet.ac.ru (V.S.); sasha-kolianova@yandex.ru (A.K.)

<sup>5</sup> A.M. Prokhorov General Physics Institute of the RAS, 119991 Moscow, Russia

<sup>6</sup> “N.N. Blokhin National Medical Research Center of Oncology” of the Ministry of Health of the Russian Federation, 119991 Moscow, Russia

<sup>7</sup> Ufa State Aviation Technical University, 450077 Ufa, Russia; giraab@mail.ru

<sup>8</sup> Institute of Materials Research, Division Metallic Biomaterials, Helmholtz-Zentrum Geesthacht (HZG), 21502 Geesthacht, Germany; Regine.Willumeit@hzg.de

<sup>9</sup> Department of Materials Science and Engineering, Monash University, 3800 Clayton, Australia; yuri.estrin@monash.edu

<sup>10</sup> Department of Mechanical Engineering, The University of Western Australia, 6009 Crawley, Australia

<sup>11</sup> Institute of Solid State Physics of the Russian Academy of Sciences, Ac. Ossipyan str., 2, 142432 Chernogolovka, Russia

\* Correspondence: [straumal@issp.ac.ru](mailto:straumal@issp.ac.ru)

Received: 17 September 2020; Accepted: 8 October 2020; Published: 10 October 2020



**Abstract:** The effect of equal channel angular pressing (ECAP) on the microstructure, texture, mechanical properties, and corrosion resistance of the alloys Mg-6.0%Ag and Mg-10.0%Gd was studied. It was shown that ECAP leads to grain refinement of the alloys down to the average grain size of 2–3  $\mu\text{m}$  and 1–2  $\mu\text{m}$ , respectively. In addition, in both alloys the precipitation of fine particles of phases  $\text{Mg}_{54}\text{Ag}_{17}$  and  $\text{Mg}_5\text{Gd}$  with sizes of ~500–600 and ~400–500 nm and a volume fraction of ~9% and ~8.6%, respectively, was observed. In the case of the alloy Mg-6.0%Ag, despite a significant grain refinement, a drop in the strength characteristics and a nearly twofold increase in ductility (up to ~30%) was found. This behavior is associated with the formation of a sharp inclined basal texture. For alloy Mg-10.0%Gd, both ductility and strength were enhanced, which can be associated with the combined effect of significant grain refinement and an increased probability of prismatic and basal glide. ECAP was also shown to cause a substantial rise of the biodegradation rate of both alloys and an increase in pitting corrosion. The latter effect is attributed to an increase in the dislocation density induced by ECAP and the occurrence of micro-galvanic corrosion at the matrix/particle interfaces.

**Keywords:** biomedical materials; magnesium alloys; equal-channel angular pressing (ECAP); microstructure; X-ray diffraction (XRD); texture; mechanical properties; biodegradation

---

## 1. Introduction

The combination of good biocompatibility and acceptable mechanical properties made magnesium alloys one of the most popular groups of materials for bioresorbable implants [1–7]. In recent years, research has been increasingly directed towards the development of magnesium alloys for medical applications. Along with good biocompatibility, these alloys often have additional functional properties. These properties, in combination with a suitable degradation rate, result from a smart selection of alloying elements. For example, it is possible to create an alloy with antibacterial activity. A medical prosthesis or implant made from such an alloy can reduce a risk of wound infection in the postoperative period due to gradual release of metal ions in combination with temporal pH changes inhibiting the growth of bacteria during the degradation of the implanted device. A good example are alloys of the Mg-Zn-Sn system. Not only do they possess good biocompatibility, but they also inhibit the growth of bacteria due to alkalization of the medium during degradation and the concomitant release of Mg, Sn, and Zn ions [8,9]. Gao et al. [10] showed that alloying magnesium with a small amount of Sr and Ga (up to 0.1 wt.%) effectively suppresses the activity of Gram-positive and Gram-negative bacteria (*Staphylococcus aureus*, *Staphylococcus epidermidis*, *Escherichia coli*), mainly due to the release of  $Ga^{3+}$  ions. Magnesium alloyed with silver also shows similar properties [11–14].

Another important area of research concerns medical magnesium alloys with an antitumor effect. Currently, development of drugs with systemic cytostatic activity for treatment of cancer patients is a truly topical area of medicine. Despite that, surgery is still one of the most used treatments. In this case, there usually is a need for partial replacement of the affected area with an artificial product. Examples include resection of bone affected by osteosarcoma or excision of a part of the esophagus. Due to their biodegradability, magnesium alloys are promising candidates for such applications. An emerging area of application of Mg alloys is oncology. Indeed, biodegradability potentially enables deployment of implants made from magnesium alloys as a platform for targeted delivery of gradually released cytostatic agents that suppress the growth and vitality of tumor cells in the area of neoplasm formation. Recent studies of medicinal magnesium alloys have been aimed at developing alloy compositions that would allow for inhibiting the vital activity of cancer cells, while not exerting a detrimental effect on normal cells. Thus, Wang et al. [15] showed that a Mg-Zn-Y-Nd alloy has a greater cytotoxicity to esophageal cancer cells than 317L stainless steel, which is frequently used in the production of stents. Studies carried out on giant cell tumors of bone incubated with samples of zoledronic acid-loaded magnesium-strontium alloys also demonstrated the advantages of this approach [16]. It was shown in [17] that the appropriate degradation of even pure magnesium leads to the inhibition of the growth of the MG63 osteosarcoma cell line, while the addition of Ag and Y enhances this effect. Studies carried out on the U2OS cancer cell line showed the effectiveness of the additions of Zn [18] and La [19] as inhibitors of cell growth, the effect being enhanced with an increase in the content of these elements. In addition, the present authors also carried out research aimed at studying the effect of the addition of rare earth elements [20] and Ag [21] on the vitality of tumor cells. These previous studies allow us to conclude that the use of magnesium alloys with an appropriate composition and degradation behavior is a promising avenue for treatment of cancer patients.

However, it should be emphasized that, quite often, the medical magnesium alloys may contain alloying elements which negatively affect their mechanical properties. This may preclude their use in medical devices. Indeed, orthopedic implants must have a sufficiently high level of strength, while stents require good ductility. Potential negative effects of alloying may be compensated for by the microstructure modification of the alloy. This can be achieved, for example, by plastic deformation imparting the desired properties to the material. From this viewpoint, equal-channel angular pressing

(ECAP) looks particularly promising [22]. Due to significant grain refinement this technique generally produces, it can improve the mechanical characteristics of metallic materials quite substantially. However, in contrast to the body-centered cubic and face-centered cubic metals, which deform well at room temperature [23–25], the low number of slip systems in magnesium and its alloys makes it necessary to carry out deformation processing at elevated temperatures. In this case, the accumulation of crystal lattice defects with a density sufficient for the formation of an ultrafine-grained (UFG) structure is hindered by the processes of recovery and recrystallization. Therefore, it is advisable to carry out ECAP with a stepwise decrease in the processing temperature for microstructure refinement [26–29] that would allow accumulation of sufficiently high dislocation density.

In this work, the effect of ECAP on the structure, texture, mechanical properties, and corrosion behavior of magnesium-based alloys Mg-6.0%Ag and Mg-10.0%Gd was studied. These alloys are attractive candidates for treatment of cancer patients. The earlier studies on alloys of the Mg-Ag [21,30] and Mg-Gd [31–33] systems showed that this deformation method is promising for the refinement of the microstructure and the associated increase in strength and ductility of alloys of these systems.

## 2. Materials and Methods

The alloys investigated, Mg-6.0%Ag and Mg-10.0%Gd, were obtained by smelting in a Nabertherm induction furnace (Nabertherm, Lilienthal, Germany) at a temperature of 720 °C using a mixture of Ar<sup>+</sup> with 3 vol.% SF<sub>6</sub> as a protective gas. Subsequently, cast ingots with a diameter of 60 mm underwent a T4 heat treatment (annealing at 425 °C for 16 h for Mg-6.0%Ag and at 525 °C for 8 h for Mg-10.0%Gd, followed by quenching in water). To obtain billets 10 mm in diameter required for ECAP, ingots of the alloys were extruded with an extrusion ratio of 1:25. The extrusion was conducted at a temperature of 425 °C and a ram speed of 1.1 mm/s for Mg-6.0%Ag alloy and at a temperature of 400 °C and a ram speed of 2.2 mm/s for Mg-10.0%Gd alloy. Before extrusion, the alloys were preheated for 60 min at deformation temperatures. After extrusion, both alloys were annealed again at a homogenization temperature (425 °C for 2 h and 525 °C for 1 h for Mg-6.0%Ag and Mg-10.0%Gd, respectively) and cooled by quenching in water. The resulting condition will be referred to as the initial state of the alloys. Route Bc ECAP was carried out with temperature being dropped in discrete steps after defined strain increments (Figure 1a). The intersection angle between the entry and exit channels of the ECAP die was 120° (Figure 1b), and the total number of passes was 12.

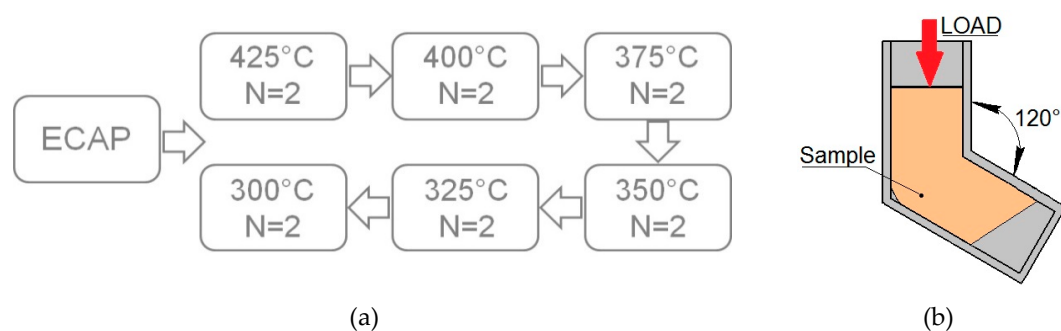


**Figure 1.** The equal channel angular pressing (ECAP) processing regime employed (a) and the scheme of ECAP process (b). N denotes the number of passes at a given temperature.

The study of the microstructure of the alloys in the initial state and after ECAP was carried out in the direction parallel to the direction of ECAP and extrusion preceding annealing for the initial state of the alloys. The microstructure of the alloys in the initial state and after ECAP was investigated using an optical microscope Axio Observer D1m (Carl Zeiss, Jena, Germany). The microstructure of alloys after ECAP was also studied by transmission electron microscopy (TEM) using a JEOL JEM 2010 microscope (Jeol, Tokyo, Japan). The operating voltage was 200 kV. The foils for TEM studies were prepared by ion-milling in a precision ion polishing system (Gatan, PIPS II, Gatan Inc. Pleasanton, CA, USA). A

quantitative assessment of structural components was carried out by the method of random secants using the software Image Expert Professional 3 (Version 3, Moscow, Russia).

Phase analysis by means of X-ray diffraction (XRD) was performed on a Rigaku Ultima IV diffractometer (Rigaku, Japan) using Co-K $\alpha$  radiation and a graphite monochromator for a diffracted beam. The spectra were analyzed using the PDXL software (Rigaku, Japan) by the Rietveld method with the PDF-2 powder diffractogram database (ICDD). Texture measurements were carried out using a DRON-7 X-ray diffractometer (SPE “Burevestnik,” St. Petersburg, Russia) in CuK $\alpha$  radiation with the aid of the Texx [34] and Texxor [35] software (IMET RAS, Moscow, Russia). Five incomplete direct pole figures {10 $\bar{1}$ 2}, {11 $\bar{2}$ 0}, {10 $\bar{1}$ 3}, {0004}, and {10 $\bar{1}$ 4} were obtained with a maximum inclination angle  $\alpha_{\max} = 70^\circ$  and a step size of  $5^\circ$  in the radial angle  $\alpha$  and the azimuth angle  $\beta$  on a pole figure. The orientation distribution functions (ODFs) were calculated from the measured pole figures presented as a superposition of a large number (1,000) of standard distributions with a small scatter. The centers of standard functions were located on a regular three-dimensional grid in the orientation space [35]. From these ODFs, complete pole figures were also calculated. The volume fractions of the major orientations were estimated using the ODF as described in [36]. Using the Euler angles and the volume fractions of the orientations, the generalized Schmid factors for the existing deformation systems and the inverse orientation factors were calculated, following the procedure reported in [36]. The texture analysis was carried out in the directions parallel and perpendicular to the pressing axis.

The mechanical properties of the alloys were evaluated based on uniaxial tensile tests carried out at room temperature in an Instron 3382 testing machine (Instron, High Wycombe, UK) with an extension rate of 1 mm/min. The tests were carried out on flat samples with a cross-section of 2 mm  $\times$  1 mm and a gauge length of 5.75 mm.

The degradation of the alloys *in vitro* was studied at 37 °C. Before testing, the samples in the form of disks 10 mm in diameter and 1.5 mm in thickness were grinded with abrasive paper (from P800 to P2500), cleaned using an ultrasonic bath, and then sterilized by immersing them for four hours in 70% ethanol and drying under sterile conditions. The specimens (no less than four for each condition) were incubated in a DMEM (Dulbecco’s Modified Eagle Medium; Sigma-Aldrich, St. Louis, MO, USA) culture medium for four days. After incubation, the specimens were rinsed in a solution of Cr<sub>2</sub>O<sub>3</sub>, AgNO<sub>3</sub>, Ba(NO<sub>3</sub>)<sub>2</sub>, and distilled water for one minute in order to remove degradation products from their surfaces. The mass loss was determined by weighing the specimens with a Sartorius Pro 11 scale (ISO 9001; Sartorius Lab Instruments GmbH & Co, Göttingen, Germany) with an accuracy of three decimal places, or 0.001 g. The degradation rate, DR (in mm/year) was calculated using the following equation (ASTM\_G1-03-E):

$$DR = 8.76 \times 10^4 \times \frac{\Delta m}{A \times t \times \rho} \quad (1)$$

where  $\Delta m$  is the mass loss in grams,  $t$  is the immersion time in hours,  $A$  is the specimen surface area in cm<sup>2</sup>, and  $\rho$  is the density of the alloy in g/cm<sup>3</sup>.

The surface of the samples after degradation tests was inspected using an instrumental microscope MMI-2 (NPZ, Novosibirsk, USSR).

### 3. Results

Figure 2 shows the microstructure of the alloys Mg-6.0%Ag and Mg-10.0%Gd in the initial state and after ECAP. The microstructure of both alloys after annealing consisted of grains of a supersaturated solid solution of silver or gadolinium in magnesium. No second-phase particle precipitation after quenching in water was detected metallographically and by XRD. The average grain size in the initial state was  $70.9 \pm 4.0 \mu\text{m}$  for the alloy Mg-6.0%Ag and  $70.8 \pm 4.0 \mu\text{m}$  for the alloy Mg-10.0%Gd (Figure 2a,b).



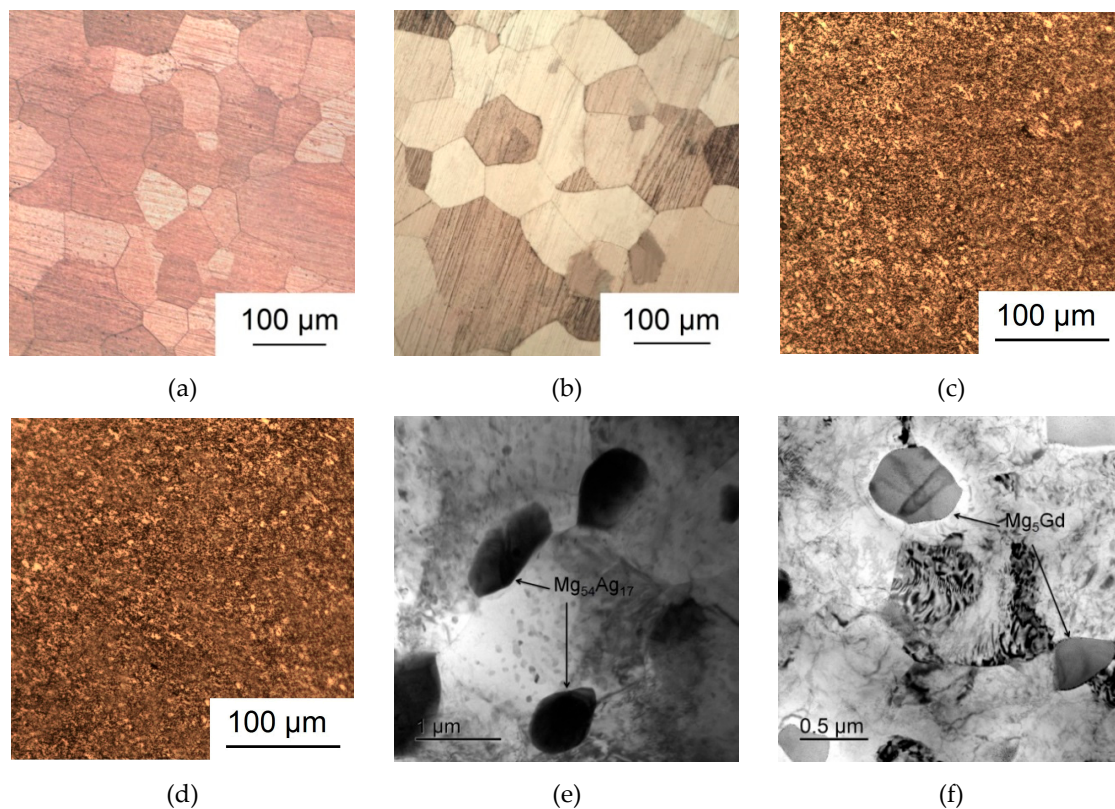


**Figure 2.** Structure of the alloys Mg-6.0%Ag (a,c,e) and Mg-10.0%Gd (b,d,f) in the initial state (a,b) and after ECAP (c–f).

ECAP led to a substantial refinement of the microstructure of both alloys. It should be noted that this microstructure was generally homogeneous without signs of bimodality (Figure 2c,d). The grain size decreased to  $\sim 2\text{--}3\ \mu\text{m}$  in the case of the Mg-6.0% Ag alloy and to  $\sim 1\text{--}2\ \mu\text{m}$  in the case of the Mg-10.0%Gd alloy. ECAP deformation conducted at elevated temperatures with cooling of the billets at room temperature led to the precipitation of second-phase particles in both alloys. In the Mg-6.0%Ag alloy, the precipitation of second-phase particles with a size of  $\sim 500\text{--}600\ \text{nm}$ , located mainly at the grain boundaries, was found. In alloy Mg-10.0%Gd, precipitation of second-phase particles was observed mainly at triple points. The particles were round and  $\sim 400\text{--}500\ \text{nm}$  in size (Figure 2e,f).

To identify the stoichiometric composition of precipitated particles and to determine their volume fraction, the XRD phase analysis of the alloys was carried out before and after deformation (Figure 3). Investigation of the Mg-6.0%Ag alloy in the initial state showed that after quenching, the alloy was entirely in a single-phase condition represented by a supersaturated solid solution of silver in magnesium. By contrast, in Mg-10.0%Gd alloy, about  $\sim 1.9\%$  of a second phase, identified as  $\text{Mg}_{46}\text{Gd}_9$ , was detected. According to our analysis, this phase had face-centered cubic structure (space group  $F\bar{4}3m$ ). In earlier studies [37] a compound with about the same stoichiometric composition was already identified as a  $\text{Mg}_5\text{Gd}$ . Furthermore, according to literature, the occurrence of this compound ( $\text{Mg}_5\text{Gd}$ ) was also identified in Mg-10.0%Gd alloy after aging treatment [38]. It can be surmised that in our case this phase was formed during the extrusion process prior to annealing and did not have enough time to dissolve during the initial heat treatment. After ECAP, the volume fraction of particles of the  $\text{Mg}_{46}\text{Gd}_9$  ( $\text{Mg}_5\text{Gd}$ ) phase was found to be about 18.6%.

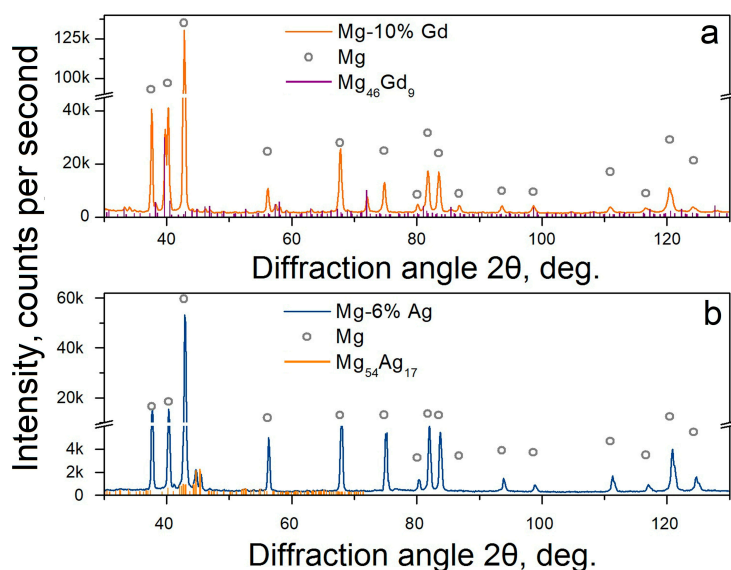


**Figure 3.** XRD spectra of the alloys Mg-10.0%Gd (a) and Mg-6.0%Ag (b) after ECAP. (Note that the  $Mg_{46}Gd_9$  phase is nearly identical with the  $Mg_5Gd$  phase).

Investigation of the Mg-6.0% Ag alloy after ECAP also showed precipitation of second-phase particles with a volume fraction of ~9%, apparently during heating process before and during the ECAP processing. We identified this phase as  $Mg_{54}Ag_{17}$  (space group Immm), which is in good agreement with the literature data [11,30,39].

Table 1 and Figure 4 show a summary of the mechanical properties of the alloys at the room temperature before and after ECAP. The yield stress (YS) of the alloy Mg-6.0%Ag in the initial state was  $162 \pm 3$  MPa and its ultimate tensile strength (UTS) was  $239 \pm 1$  MPa. After ECAP, a drop in these characteristics to  $44 \pm 6$  MPa and  $224 \pm 5$  and, respectively, was observed. At the same time, tensile elongation (El) of the alloy after ECAP rose to  $30.6 \pm 3.0\%$  - to be compared to  $16.0 \pm 0.3\%$  in the initial state. By contrast, ECAP of Mg-10.0%Gd led to an increase in both strength and ductility characteristics. The respective values of YS, UTS, and El rose from  $123 \pm 7$  MPa,  $185 \pm 4$  MPa, and  $13.2 \pm 1.7\%$  in the initial state to  $211 \pm 1$  MPa,  $258 \pm 2$  MPa, and  $18.0 \pm 3.6\%$  in the post-ECAP condition.

**Table 1.** Mechanical properties of the Mg-6.0%Ag and Mg-10.0%Gd alloys before and after ECAP.

Processing		YS, MPa	UTS, MPa	El, %	Grain Size, $\mu\text{m}$
Mg-6.0%Ag	Initial state	$162 \pm 3$	$239 \pm 1$	$16.0 \pm 0.3$	$70.9 \pm 4.0$
	ECAP	$44 \pm 6$	$224 \pm 5$	$30.6 \pm 3.0$	2–3
Mg-10.0%Gd	Initial state	$123 \pm 7$	$185 \pm 4$	$13.2 \pm 1.7$	$70.8 \pm 4.0$
	ECAP	$211 \pm 1$	$258 \pm 2$	$18.0 \pm 3.6$	1–2

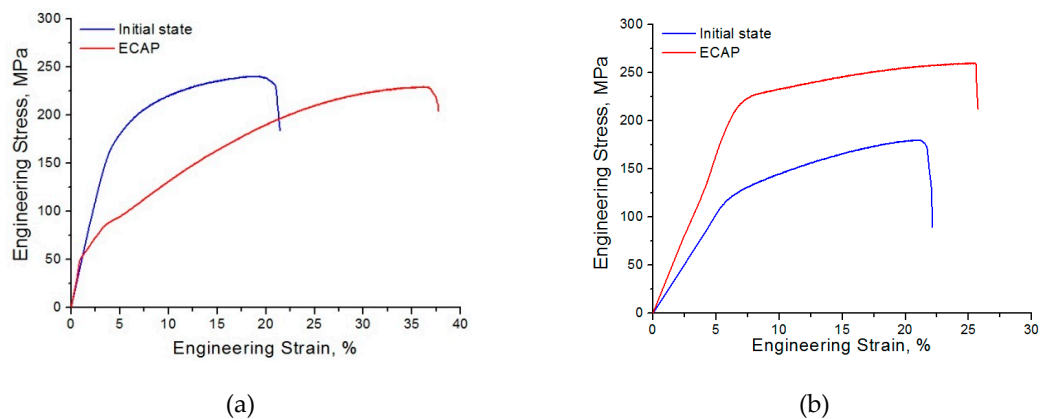


**Figure 4.** Engineering stress–strain response of the alloys Mg-6.0%Ag (a) and Mg-10.0%Gd (b) before and after ECAP.

It should also be noted that for the Mg-10.0%Gd alloy processed by ECAP the elastic portion of the engineering stress vs. engineering strain curve has a greater slope than for the alloy in the initial condition (Figure 4b). We believe that the reason for such behavior is an increase in Young's modulus due to texture and structure transformations that occur in the alloy after ECAP deformation. Our calculations (to be presented in forthcoming publications) confirm this hypothesis at a qualitative level. Another interesting issue for discussion is the occurrence of an inflection in the deformation curve for alloy Mg-6.0%Ag after ECAP (Figure 4a). This behavior (also observed for Mg-4.0%Ag deformed in compression [30]) may be associated with the activation of new slip systems during uniaxial tension or deformation twinning. While the latter mechanism cannot be ruled out on theoretical grounds, no twins were detected in the ECAP-processed Mg-6.0%Ag after uniaxial tension. At this stage, the question of the mechanism responsible for the occurrence of the inflection remains open.

In addition to the influence of ECAP on the mechanical characteristics through microstructure changes, the texture variation usually also comes into play. Therefore, we conducted texture measurements in the initial state and after ECAP (both in the longitudinal and the transversal sections of the billets) (Figure 5). The pole figures (PFs) of Mg-6.0%Ag exhibited a transformation from a sharp prismatic texture in the initial state to an inclined basal one. The inclination angle  $\alpha = 45\text{--}50^\circ$  relative to the longitudinal direction (LD) and a rotation angle  $\beta = 25\text{--}30^\circ$  relative to the normal direction (ND) clockwise in the cross-section of the billet were found after ECAP (see pole figure (PF) {0004} in Figure 5a). The texture in the longitudinal section of the billet in the initial state was a rather weak prismatic type. It transformed to a sharp basal texture inclined at  $\alpha = 85^\circ$  relative to ND and rotated by an angle  $\beta = 45^\circ$  relative to LD counterclockwise after ECAP (see PF {0004} in Figure 5b). Unlike this texture behavior, the texture of the alloy Mg-10.0%Gd in the initial and the post-ECAP condition was rather dispersed and did not exhibit sharp peaks, neither in the longitudinal nor in the transversal section of the billets (Figure 5c,d).

The results on the degradation rate for both alloys studied in the initial state and after ECAP are presented in Figure 6a. These data show that the microstructure changes and modification of phase composition occurring as a result of ECAP lead to an increase in the degradation rate. Thus, the degradation rate of the alloy Mg-6.0%Ag after ECAP rose to  $3.74 \pm 0.56$  mm/year compared to  $0.43 \pm 0.10$  mm/year in the initial state. In the case of the Mg-10.0%Gd alloy, an increase in the degradation rate from  $0.15 \pm 0.04$  mm/year in the initial state to  $2.19 \pm 0.78$  mm/year after ECAP was observed.

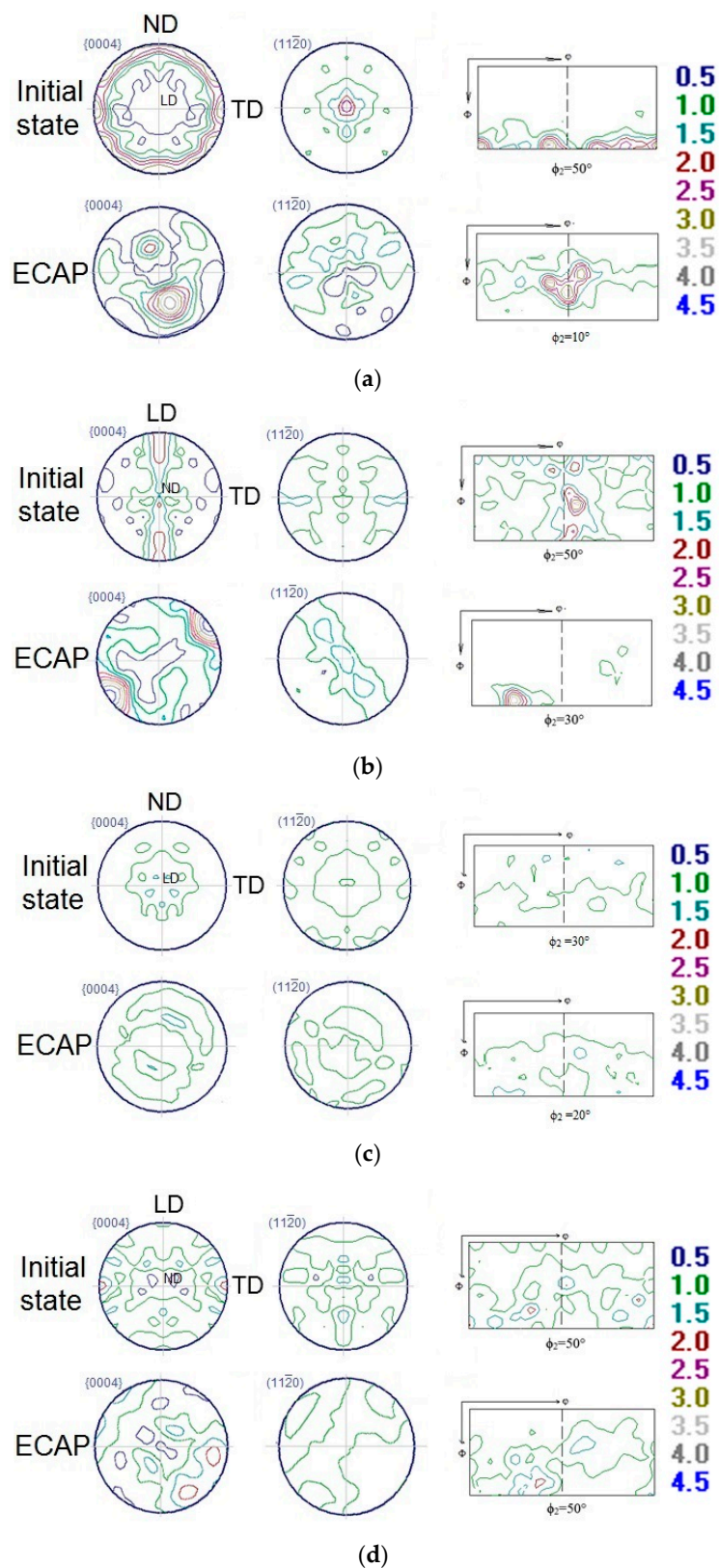
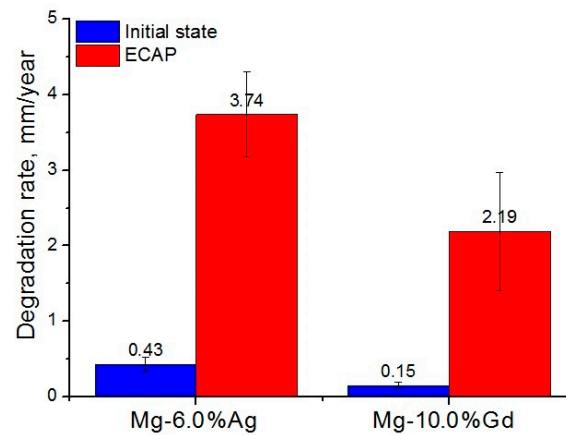
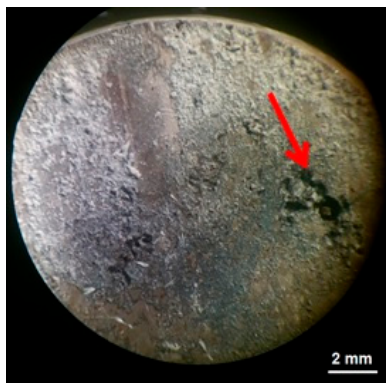


**Figure 5.**  $\{0004\}$  and  $\{11\bar{2}0\}$  pole figures and cross-sections of orientation distribution functions (ODF) of the Mg-6.0%Ag (a,b) and Mg-10.0%Gd (c,d) alloys in the initial state and after ECAP for transversal (a,c) and longitudinal (b,d) sections of billets. (The notation LD, TD, and ND corresponds to the longitudinal, transverse, and normal direction, respectively).





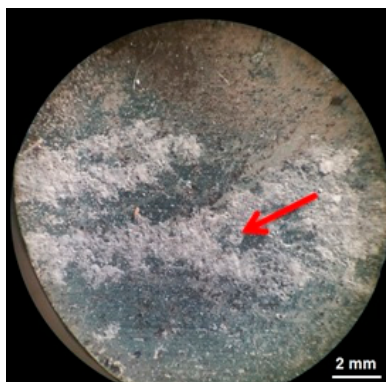
(a)



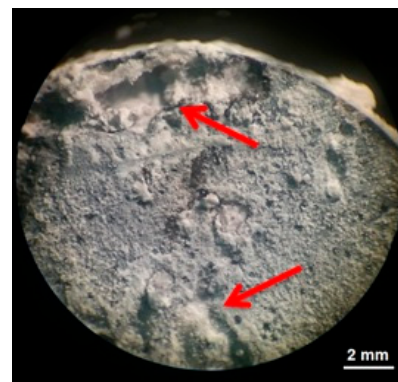
(b)



(c)



(d)



(e)

**Figure 6.** Degradation rate (a) and the surface of the samples after testing but before cleaning for alloy Mg-6.0%Ag (b,c) and alloy Mg-10.0%Gd (d,e). The images (b,d) correspond to the initial state and (c,e) to the post-ECAP state of the respective alloys. The arrows indicate sites of localized degradation.

Inspection of the sample surface after degradation tests showed nonuniformity of degradation of Mg-6.0%Ag in the initial state and especially after ECAP (Figure 6b,c). Samples of annealed Mg-6.0%Ag did show signs of localization of degradation but, unlike in the post-ECAP condition, pitting did not have a through-thickness character. In the case of the Mg-10.0%Gd alloy, nonuniform degradation was observed only in the post-ECAP samples (Figure 6e). Only minor signs of localization of corrosion were detected. To summarize these results, one can state that localization of degradation was most pronounced in the Mg-6.0%Ag alloy processed by ECAP. In this case, a profuse through-thickness pitting of samples was observed. For the ECAP-processed Mg-10.0%Gd alloy, a strong localization

of corrosion was also found, but pitting was not as expressed as in the case of the ECAP-processed Mg-6.0%Ag alloy.

The observed acceleration of the biodegradation rate of both alloys due to ECAP would generally be regarded as an undesirable effect, which would put in question the usefulness of this processing for medical implant applications of the alloys considered. However, the situation is entirely different for specifically targeted applications in oncological patients. Here, a bioresorbable implant is used not only as a mechanically strong scaffold, but also as a therapeutic agent inhibiting the growth and proliferation of tumor cells. It should also be stated that the increase in degradation rate is still relatively moderate, which in the long run is tolerated by the healthy tissue [40].

#### 4. Discussion

The studies reported here have shown that ECAP has a strong effect on the mechanical and biodegradation characteristics of magnesium alloys Mg-6.0%Ag and Mg-10.0%Gd. The effect is different for the two alloys, though. In the case of Mg-10.0%Gd, a typical situation is found: a decrease in the grain size and precipitation of second-phase particles lead to an increase in the yield strength and the ultimate tensile strength. A different picture is observed for the Mg-6.0%Ag alloy. In this case, ECAP leads to grain refinement to a scale similar to that observed in the Mg-10.0%Gd alloy. The size of the precipitated particles has a similar magnitude, as well. However, in the case of ECAP-processed Mg-6.0%Ag alloy, a decrease in both strength characteristics (both YS and UTS) is observed. On a positive side, doubling of the tensile elongation that characterizes ductility of the alloy is achieved (Figure 4, Table 1). In the case of Mg-10.0%Gd, an increase in ductility is also observed, but it is not as significant as for Mg-6.0%Ag. The most likely reason for this behavior is a change in texture induced by ECAP. As was shown for Mg-6.0%Ag, a sharp inclined basal texture occurred as a result of ECAP (Figure 5a,b). The formation of an inclined basal texture in magnesium alloys is known to have a negative effect on their strength, while having a beneficial effect on ductility. This is what was observed for the Mg-6.0%Ag alloy. A similar behavior was already found for binary Mg-2.0%Ag and Mg-4.0%Ag alloys [11] and the ternary Mg-1.0%Zn-0.3%Ca alloy [41]. A negative effect of the inclined basal texture on the yield stress was previously shown for the alloys AZ31 [42] and AM60 [43]. In the case of the Mg-10.0%Gd alloy considered here, the texture did not undergo significant changes; a weak texture in the initial state did not change its dispersed character as a result of ECAP (Figure 5c,d). However, the magnitude of the orientation factors calculated for the basal, prismatic, and pyramidal slip systems, as well as one of the main twinning systems in magnesium alloys,  $\{10\bar{1}2\}\langle\bar{1}011\rangle$ , can provide an explanation for the observed increase in ductility.

Texture orientation factors for slip systems are determined by the values of the respective Schmid factors and are their reciprocals. Therefore, a decrease in the value of an orientation factor may indicate an increase in the probability of dislocation glide on the corresponding slip system. In our case, the estimation of the orientation factors for the Mg-10.0%Gd alloy before and after ECAP, calculated for the longitudinal section of the billet, indicates the highest probability of dislocation slip on the basal planes. Indeed, the orientation factor does not show big changes, while slip on other planes weakens (Table 2). At the same time, the calculation of the orientation factors for the cross-section of the billet indicates an increase in the probability of prismatic slip, as reflected in a decrease in the value of the respective orientation factor. An increase in the probability of slip on prismatic planes can be the reason for a slight rise of the ductility of the Mg-10.0%Gd alloy. We have already observed a similar effect on a magnesium alloy with Y and Nd treated by ECAP [44]. An improvement of the ductility of magnesium alloys due to the formation of a prismatic texture was also demonstrated earlier for the quaternary Mg-4.4%Al-0.9%Zn-0.4%Mn alloy [45]. In the case of the Mg-6.0%Ag alloy, the calculation of the orientation factors indicates the most probable slip of dislocations mainly on the basal planes, which is also confirmed by the type of the observed texture. However, it should be noted that this trend is most clearly expressed in the transversal cross section of the billet. The calculation of the orientation

factors for the twinning system  $\{10\bar{1}2\}\langle\bar{1}011\rangle$  for both alloys showed a decrease in the probability of twinning, which was confirmed by the absence of twins in the structure of both alloys after ECAP.

**Table 2.** Orientation factors for deformation systems of the alloys studied. (The abbreviations CS and LS stand for a (transversal) cross section and a longitudinal section, respectively).

State of the Alloys		Basal $\{0001\}\langle 1120\rangle$	Prismatic $\{1010\}\langle 1120\rangle$	Pyramidal $\langle c+a\rangle$	Twinning $\{10\bar{1}2\}\langle\bar{1}011\rangle$	
Mg-6.0%Ag	CS	Initial state	7.5	3.6	4.9	4.7
		ECAP	4.0	5.1	5.3	5.9
	LS	Initial state	4.7	5.1	4.4	4.4
		ECAP	4.3	5.1	5.1	5.5
Mg-10.0%Gd	CS	Initial state	4.7	5.7	5.1	5.3
		ECAP	4.9	5.3	5.9	6.6
	LS	Initial state	4.5	4.7	4.9	5.0
		ECAP	4.5	5.1	5.0	5.2

The homogeneity of the microstructure of both alloys processed by ECAP suggests that the observed changes in their mechanical characteristics are associated with the structure refinement, precipitation of particles, and texture evolution. The calculation of the orientation factors shows that the basal slip prevails in the ECAP-modified alloy Mg-6%Ag. This holds true both for a longitudinal section of a processed billet (parallel to the direction of the tensile tests conducted to determine the mechanical characteristics) and for a transversal cross section of the billet. In the case of Mg-10%Gd, the magnitude of the calculated orientation factors indicates the activation of non-basal sliding. This assertion is valid only for the longitudinal section of the billet. It can be considered as established that for the alloy Mg-6%Ag the mechanical characteristics are primarily affected by texture effects, microstructure refinement and particle precipitation playing a subordinate role. By contrast, for the alloy Mg-10%Gd all three factors appear to influence the mechanical properties in accord. The combined effect of grain refinement and precipitation of particles of the  $Mg_5Gd$  phase (with the volume fraction of about 19%) is responsible for strengthening, while the activation of prismatic sliding accounts for an enhancement of ductility. However, it is known that the greatest strengthening effect after aging is observed in alloys containing from 10 to 20 wt.% Gd [46]. At the same time, the aging of the quenched alloy Mg-10%Gd has a little effect on its Vickers hardness [47], which in our case indicates that the contribution of grain refinement to strengthening still prevails over the contribution of particles. It is interesting that the equilibrium phase of  $Mg_5Gd$  precipitates in the form of plates parallel to prismatic planes  $\{10\bar{1}0\}_{Mg}$  at the early stages of aging [46,48]. In our case, the main process of nucleation of phase particles is apparently observed at the initial stages of ECAP (sequentially through the nucleation of phases  $\beta'' (Mg_3Gd) \rightarrow \beta' (Mg_{3-5}Gd) \rightarrow \beta_1 (Mg_{3-5}Gd) \rightarrow \beta (Mg_5Gd)$ ), but the coagulation and particle growth occurs with an increase in the number of passes (and, consequently, the number of heating before and during deformation). In the final state (after 12 ECAP passes), we mostly deal with large, rounded overaged particles, but we do not exclude the possibility of presence of small number of lamellar particles. At the same time, the studies carried out on the Mg-1.5Sn-1.4Zn-0.2Mn alloy with the addition of 0.3Ag indicated the formation of the particles  $\epsilon' (Mg_{54}Ag_{17})$  [49]. These particles were rod-shaped and was normal to  $(0001)_{Mg}$ . Probably, in our case, there can also be a fraction of fine particles  $\epsilon'$ , which inhibit dislocation slip, but the most part of the phase in the structure of the alloy Mg-6%Ag after ECAP is a rounded coagulated  $Mg_{54}Ag_{17}$  particle ~500–600 nm in size (Figure 2e).

The study of the corrosion properties of the alloys showed that ECAP leads to a significant acceleration of the degradation process for both Mg-6.0%Ag and Mg-10.0%Gd alloys. The reason for the recorded increase in the degradation rate is the structural and phase changes occurring in the alloys

during severe plastic deformation. On the one hand, grain refinement leads to a significant increase in the grain boundary area and in the density of dislocations. It is known that an increase in the dislocation density in metals and alloys often leads to a deterioration of their corrosion resistance [50,51]. Magnesium and its alloys are no exception to that rule. Thus, it was previously shown that grain refinement in pure magnesium caused by ECAP leads to an increase in its degradation rate and the formation of deeper pitting owing to a greater density of crystal lattice defects [51]. In the case of the ternary Mg-4.0%Zn-2.0%Ni alloy, it was shown that an increase in the extrusion temperature, which promotes a decrease in the dislocation density, led to a reduction of the degradation rate [52]. It was also shown that a reduced density of dislocations in the alloy LAZ832-0.2%Zr after extrusion is also one of the reasons for its good corrosion resistance [53]. On the other hand, there are also a number of reports asserting that the formation of an ultrafine-grained (UFG) structure in magnesium alloys can reduce the degradation rate due to the accelerated formation of a protective oxide-hydroxide layer and an ensuing increase of corrosion resistance [54–56]. However, it should be noted that no UFG structure was formed in the alloys studied. In the case of the Mg-4.0%Zn-2.0%Ni and LAZ832-0.2%Zr alloys, the dislocation density played an important role in the degradation rate. However, it was not the only factor governing the magnitude of the degradation rate. The occurrence of a second phase in the structure and its distribution affected the corrosion resistance substantially. It is known that the presence of more corrosion-resistant phases in magnesium alloys can lead to micro-galvanic corrosion, when a less resistant matrix acts as an anode, and second-phase particles act as a cathode. In our case, an increase in the degradation rate for both alloys was accompanied by the precipitation of particles of a second phase:  $Mg_{54}Ag_{17}$  in the Mg-6.0%Ag alloy and  $Mg_5Gd$  in the Mg-10.0%Gd alloy. That is, particles of  $Mg_{54}Ag_{17}$  and  $Mg_5Gd$  phases, acting as a cathode in relation to the less stable magnesium matrix, lead to an increase in the degradation rate of the alloys studied. At the same time, accelerated degradation, predominantly at the matrix/particle interface, can also promote a stronger localization of corrosion, as was observed for ECAP-treated alloys. Such behavior was also found for other magnesium alloys. For example, in the case of binary Mg-Sc alloys, an increase in the Sc content to 0.3 wt% led to an improvement of corrosion resistance, while a further increase in the Sc content led to the precipitation of Mg-Sc particles and an increase in the degradation rate by galvanic corrosion [57]. Similar behavior was demonstrated for Mg-Bi-Al-based alloys [58], Mg-6.0%Gd-2.0%Y-1.0%Zn-0.3%Zr alloy [59], Mg-Li-Ca alloys [60], etc. Not only does the micro-galvanic mechanism of corrosion cause the degradation of the matrix in the immediate vicinity of the particles, but it also causes grain-boundary corrosion if the precipitate particles reside at grain boundaries. For both alloys considered in this paper, the particle sites were the same. In addition, the formation of a protective film during corrosion of magnesium alloys was observed, mainly consisting of degradation products and compounds formed during the reaction with components of the corrosive medium. Although this film protects against degradation, it is rather unevenly distributed over the surface of the sample, often leaving unprotected spots. In such particle locations degradation proceeds at an accelerated rate, first around a particle, and then along the grain boundaries. In this case, separation of a grain (and sometimes of several grains) from the sample surface can occur, which entails the formation of pitting. Pits of this kind were observed especially clearly for alloys processed by ECAP, where the concentration of the second phase was high. The micro-galvanic mechanism of corrosion and grain-boundary corrosion of magnesium alloys are described in several works, for example, in [61–63].

Thus, the increase in the degradation rate of the Mg-6.0%Ag and Mg-10.0%Gd alloys after ECAP can be explained by a deformation-induced increase in the density of crystal lattice defects and the precipitation of second-phase particles, which promoted the occurrence of micro galvanic corrosion. Therefore, a potential way to improve the properties of Mg-based alloys, including their corrosion resistance, should focus on developing regimes of deformation in which precipitation of particles would be suppressed, or their amount would be minimized. This can be realized by lowering the initial deformation temperature, reducing the number and duration of heating cycles before and during ECAP, as well as reducing the number of deformation steps and the associated temperature drops. A



suitable method to reduce the dislocation density can be the use of low-temperature annealing after ECAP (below the temperature corresponding to the onset of active decomposition of a supersaturated solid solution). In trying to optimize the properties of the alloys one should bear in mind their intended application in bioresorbable implants. Hence, processing regimes need to be tuned to ensure the level of the degradation rate desirable for a given implant application.

## 5. Conclusions

1. Processing by ECAP was shown to cause a decrease in the average grain size down to 2–3  $\mu\text{m}$  for the Mg-6.0%Ag alloy and 1–2  $\mu\text{m}$  for the Mg-10.0%Gd alloy. In addition, ECAP-induced precipitation of particles of the  $\text{Mg}_{54}\text{Ag}_{17}$  and  $\text{Mg}_5\text{Gd}$  phases with a size of 500–600 nm and 400–500 nm and a volume fraction of  $\sim 9$  and  $\sim 18.6\%$ , respectively, was observed.
2. ECAP was also found to lead to an increase in both strength and ductility of the Mg-10.0%Gd alloy. In the case of the Mg-6.0%Ag alloy, a decrease in the UTS and especially in the YS was observed. This was accompanied with an almost twofold increase in tensile ductility as represented by the strain to failure: from  $16.0 \pm 0.3\%$  in the initial state to  $30.6 \pm 3.0\%$  after ECAP.
3. An increase in the ductility of the Mg-6.0%Ag alloy combined with a decrease in the strength characteristics is associated with the formation of a sharp inclined basal texture and the predominant slip of dislocations on the basal planes. The improvement in the ductility of the Mg-10.0%Gd alloy achieved by ECAP is associated with an increase in the probability of dislocation slip on prismatic planes, with a retained high probability of slip on the basal planes.
4. For both alloys studied, ECAP led to a significant increase in the biodegradation rate and to a pronounced pitting. In the case of the Mg-6.0%Ag alloy, the degradation rate increased from  $0.43 \pm 0.10$  mm/year in the initial state to  $3.74 \pm 0.56$  mm/year after ECAP. For the Mg-10.0%Gd alloy, the degradation rate after ECAP increased to  $2.19 \pm 0.78$  mm/year compared to  $0.15 \pm 0.04$  mm/year in the initial state. The observed rise of the degradation rate after ECAP is associated with an increase in the dislocation density after deformation and the occurrence of micro galvanic corrosion due to the precipitation of particles of the  $\text{Mg}_{54}\text{Ag}_{17}$  and  $\text{Mg}_5\text{Gd}$  phases.

The pronounced ECAP-induced rise of the biodegradation rate is undesirable for many medical applications. However, this property can be useful for obtaining alloys considered as a platform for local delivery of anticancer agents to reduce the tumor volume or to prevent recurrence of tumor growth in cancer patients. Indeed, the associated accelerated release of alloying elements with potential antitumor activity directly into the area of tumor growth can be considered as an additional remedy in antitumor therapy, complementing the standard course of systemic therapy.

**Author Contributions:** Conceptualization, B.S., Y.E. and R.W.-R.; Methodology, N.M., N.A., N.T., I.S., G.R. and V.S.; Software, N.M., N.T., G.R., A.K. and I.S.; Validation, M.K. and S.D.; Formal Analysis, B.S., S.D., Y.E. and R.W.-R.; Investigation, N.M., N.A., D.T., N.T., A.K., I.S. and V.S.; Resources, Y.E., S.D. and R.W.-R.; Data Curation, Y.E., B.S. and R.W.-R.; Writing—Original Draft Preparation, N.M.; Writing, Review and Editing, Y.E., S.D. and R.W.-R.; Visualization, N.M. and B.S.; Supervision, Y.E.; Project Administration, B.S. and R.W.-R.; Funding Acquisition, B.S. and R.W.-R. All authors have read and agreed to the published version of the manuscript.

**Funding:** This research was funded through RSF grant # 18-45-06010 and Helmholtz-RSF Joint Research Groups Grant (Grant # HRSF-0025).

**Acknowledgments:** Our thanks go to B. Wiese who supplied the Mg-6.0%Ag and Mg-10.0%Gd alloys used in this work.

**Conflicts of Interest:** The authors declare no conflict of interest.

## References

1. Han, H.-S.; Loffredo, S.; Jun, I.; Edwards, J.; Kim, Y.-C.; Seok, H.-K.; Witte, F.; Mantovani, D.; Glyn-Jones, S. Current status and outlook on the clinical translation of biodegradable metals. *Mater. Today* **2019**, *23*, 57–71. [[CrossRef](#)]
2. Zheng, Y.; Gu, X.; Witte, F. Biodegradable metals. *Mater. Sci. Eng. R Rep.* **2014**, *77*, 1–34. [[CrossRef](#)]

3. Parfenov, E.; Kulyasova, O.; Mukaeva, V.; Mingo, B.; Farrakhov, R.; Cherneikina, Y.; Yerokhin, A.; Zheng, Y.; Valiev, R. Influence of ultra-fine grain structure on corrosion behaviour of biodegradable Mg-1Ca alloy. *Corr. Sci.* **2020**, *163*, 108303. [[CrossRef](#)]
4. Kiani, F.; Wen, C.; Li, Y. Prospects and strategies for magnesium alloys as biodegradable implants from crystalline to bulk metallic glasses and composites—A review. *Acta Biomater.* **2020**, *103*, 1–23. [[CrossRef](#)]
5. Costantino, M.; Schuster, A.; Helmholz, H.; Meyer-Rachner, A.; Willumeit-Römer, R.; Luthringer-Feyerabend, B.J. Inflammatory response to magnesium-based biodegradable implant materials. *Acta Biomater.* **2020**, *101*, 598–608. [[CrossRef](#)]
6. Merson, D.L.; Brilevesky, A.; Myagkikh, P.; Tarkova, A.; Prokhorikhin, A.; Kretov, E.; Frolova, T.S.; Vinogradov, A. The Functional Properties of Mg–Zn–X Biodegradable Magnesium Alloys. *Materials* **2020**, *13*, 544. [[CrossRef](#)] [[PubMed](#)]
7. Bazhenov, V.E.; Kolytgin, A.; Komissarov, A.; Li, A.; Bautin, V.; Khasenova, R.; Anishchenko, A.; Seferyan, A.; Komissarova, J.; Estrin, Y. Gallium-containing magnesium alloy for potential use as temporary implants in osteosynthesis. *J. Magnes. Alloy.* **2020**, *8*, 352–363. [[CrossRef](#)]
8. Zhao, W.; Wang, J.; Weiyang, J.; Qiao, B.; Wang, Y.; Li, Y.; Jiang, D.-M. A novel biodegradable Mg-1Zn-0.5Sn alloy: Mechanical properties, corrosion behavior, biocompatibility, and antibacterial activity. *J. Magnes. Alloy.* **2020**, *8*, 374–386. [[CrossRef](#)]
9. Jiang, W.; Wang, J.; Liu, Q.; Zhao, W.; Jiang, D.; Guo, S. Low hydrogen release behavior and antibacterial property of Mg-4Zn-xSn alloys. *Mater. Lett.* **2019**, *241*, 88–91. [[CrossRef](#)]
10. Gao, Z.; Song, M.; Liu, R.-L.; Shen, Y.; Ward, L.; Cole, I.; Chen, X.; Liu, X. Improving in vitro and in vivo antibacterial functionality of Mg alloys through micro-alloying with Sr and Ga. *Mater. Sci. Eng. C* **2019**, *104*, 109926. [[CrossRef](#)]
11. Tie, D.; Feyerabend, F.; Müller, W.D.; Schade, R.; Liefeth, K.; Kainer, K.; Willumeit, R. Antibacterial biodegradable Mg-Ag alloys. *Eur. Cells Mater.* **2013**, *25*, 284–298. [[CrossRef](#)] [[PubMed](#)]
12. Feng, Y.; Zhu, S.; Wang, L.; Chang, L.; Hou, Y.; Guan, S. Fabrication and characterization of biodegradable Mg-Zn-Y-Nd-Ag alloy: Microstructure, mechanical properties, corrosion behavior and antibacterial activities. *Bioact. Mater.* **2018**, *3*, 225–235. [[CrossRef](#)] [[PubMed](#)]
13. Shuai, C.; Zhou, Y.; Yang, Y.; Gao, C.; Peng, S.; Wang, G. Ag-Introduced Antibacterial Ability and Corrosion Resistance for Bio-Mg Alloys. *BioMed Res. Int.* **2018**, *2018*, 1–13. [[CrossRef](#)] [[PubMed](#)]
14. Dai, Y.; Liu, H.; Tang, Y.; Xu, X.; Long, H.; Yan, Y.; Luo, Z.; Zhang, Y.; Yu, K.; Zhu, Y. A Potential Biodegradable Mg-Y-Ag Implant with Strengthened Antimicrobial Properties in Orthopedic Applications. *Metals* **2018**, *8*, 948. [[CrossRef](#)]
15. Wang, S.; Zhang, X.; Li, J.; Liu, C.; Guan, S. Investigation of Mg–Zn–Y–Nd alloy for potential application of biodegradable esophageal stent material. *Bioact. Mater.* **2020**, *5*, 1–8. [[CrossRef](#)] [[PubMed](#)]
16. Li, M.; Wang, W.; Zhu, Y.; Lu, Y.; Wan, P.; Yang, K.; Zhang, Y.; Mao, C. Molecular and cellular mechanisms for zoledronic acid-loaded magnesium-strontium alloys to inhibit giant cell tumors of bone. *Acta Biomater.* **2018**, *77*, 365–379. [[CrossRef](#)]
17. Dai, Y.; Tang, Y.; Xu, X.; Luo, Z.; Zhang, Y.; Li, Z.; Lin, Z.; Zhao, S.; Zeng, M.; Sun, B.; et al. Evaluation of the mechanisms and effects of Mg–Ag–Y alloy on the tumor growth and metastasis of the MG63 osteosarcoma cell line. *J. Biomed. Mater. Res. Part B Appl. Biomater.* **2019**, *107*, 2537–2548. [[CrossRef](#)]
18. Wu, Y.; He, G.; Zhang, Y.; Liu, Y.; Li, M.; Wang, X.; Li, N.; Li, K.; Zheng, G.; Zheng, Y.; et al. Unique antitumor property of the Mg-Ca-Sr alloys with addition of Zn. *Sci. Rep.* **2016**, *6*, 21736. [[CrossRef](#)]
19. Shuai, C.; Liu, L.; Shuai, C.; Gao, C.; Zhao, M.-C.; Yi, L.; Peng, S. Lanthanum-Containing Magnesium Alloy with Antitumor Function Based on Increased Reactive Oxygen Species. *Appl. Sci.* **2018**, *8*, 2109. [[CrossRef](#)]
20. Anisimova, N.; Kiselevskiy, M.; Martynenko, N.; Straumal, B.; Willumeit-Römer, R.; Dobatkin, S.; Estrin, Y. Cytotoxicity of biodegradable magnesium alloy WE43 to tumor cells in vitro: Bioresorbable implants with antitumor activity? *J. Biomed. Mater. Res. Part B Appl. Biomater.* **2019**, *108*, 167–173. [[CrossRef](#)]
21. Estrin, Y.; Martynenko, N.; Anisimova, N.; Temralieva, D.; Kiselevskiy, M.; Serebryany, V.; Raab, G.; Straumal, B.; Wiese, B.; Willumeit-Römer, R.; et al. The Effect of Equal-Channel Angular Pressing on the Microstructure, the Mechanical and Corrosion Properties and the Anti-Tumor Activity of Magnesium Alloyed with Silver. *Materials* **2019**, *12*, 3832. [[CrossRef](#)] [[PubMed](#)]
22. Valiev, R.; Langdon, T.G. Principles of equal-channel angular pressing as a processing tool for grain refinement. *Prog. Mater. Sci.* **2006**, *51*, 881–981. [[CrossRef](#)]

23. Muñoz, J.A.; Higuera, O.F.; Cabrera-Marrero, J.-M. Microstructural and mechanical study in the plastic zone of ARMCO iron processed by ECAP. *Mater. Sci. Eng. A* **2017**, *697*, 24–36. [[CrossRef](#)]
24. Bochar, N.; Rybalchenko, O.V.; Shangina, D.; Dobatkin, S. Effect of equal-channel angular pressing on the precipitation kinetics in Cu-Cr-Hf alloys. *Mater. Sci. Eng. A* **2019**, *757*, 84–87. [[CrossRef](#)]
25. Rybal'Chenko, O.; Dobatkin, S.; Kaputkina, L.; Raab, G.; Krasilnikov, N. Strength of ultrafine-grained corrosion-resistant steels after severe plastic deformation. *Mater. Sci. Eng. A* **2004**, 387–389. [[CrossRef](#)]
26. Bryła, K. Microstructure and mechanical characterisation of ECAP-ed ZE41A alloy. *Mater. Sci. Eng. A* **2020**, *772*, 138750. [[CrossRef](#)]
27. Li, W.; Shen, Y.; Shen, J.; Shen, D.; Liu, X.; Zheng, Y.; Yeung, K.W.; Guan, S.; Kulyasova, O.B.; Valiev, R.Z. In vitro and in vivo studies on pure Mg, Mg–1Ca and Mg–2Sr alloys processed by equal channel angular pressing. *Nano Mater. Sci.* **2020**, *2*, 96–108. [[CrossRef](#)]
28. Martynenko, N.; Lukyanova, E.; Anisimova, N.; Kiselevskiy, M.; Serebryany, V.; Yurchenko, N.; Raab, G.; Birbilis, N.; Salishchev, G.; Dobatkin, S.; et al. Improving the property profile of a bioresorbable Mg-Y-Nd-Zr alloy by deformation treatments. *Materialia* **2020**, *13*, 100841. [[CrossRef](#)]
29. Minárik, P.; Veselý, J.; Král, R.; Bohlen, J.; KUBÁSEK, J.; Janeček, M.; Stráská, J. Exceptional mechanical properties of ultra-fine grain Mg-4Y-3RE alloy processed by ECAP. *Mater. Sci. Eng. A* **2017**, *708*, 193–198. [[CrossRef](#)]
30. Bryła, K.; Horáky, J.; Krystian, M.; Lityńska-Dobrzyńska, L.; Mingler, B. Microstructure, mechanical properties, and degradation of Mg-Ag alloy after equal-channel angular pressing. *Mater. Sci. Eng. C* **2020**, *109*, 110543. [[CrossRef](#)]
31. Alizadeh, R.; Ngan, A.H.W.; Pereira, P.H.R.; Huang, Y.; Langdon, T.G.; Mahmudi, R. Microstructure, Texture, and Superplasticity of a Fine-Grained Mg-Gd-Zr Alloy Processed by Equal-Channel Angular Pressing. *Met. Mater. Trans. A* **2016**, *47*, 6056–6069. [[CrossRef](#)]
32. Fu, Y.; Sun, J.; Yang, Z.; Xu, B.; Han, J.; Chen, Y.; Jiang, J.; Ma, A. Aging behavior of a fine-grained Mg-10.6Gd-2Ag alloy processed by ECAP. *Mater. Charact.* **2020**, *165*, 110398. [[CrossRef](#)]
33. Sun, J.; Xu, B.; Yang, Z.; Zhou, H.; Han, J.; Wu, Y.; Song, D.; Yuan, Y.; Zhuo, X.; Liu, H.; et al. Achieving excellent ductility in high-strength Mg-10.6Gd-2 Ag alloy via equal channel angular pressing. *J. Alloy. Compd.* **2020**, *817*, 152688. [[CrossRef](#)]
34. Serebryany, V.N.; Kurtasov, S.F.; Savyolova, T. Pole Figure Measurement Plan Influence on Accuracy ODF Coefficients Determined by Modified Harmonic Method. *Mater. Sci. Forum* **2005**, *495*, 1693. [[CrossRef](#)]
35. Savyolova, T.; Kourtasov, S. ODF Restoration by Orientations Grid. *Mater. Sci. Forum* **2005**, *495*, 301–306. [[CrossRef](#)]
36. Serebryany, V.N.; Rokhlin, L.L.; Monina, A.N. Texture and anisotropy of mechanical properties of the magnesium alloy of Mg-Y-Gd-Zr system. *Inorg. Mater. Appl. Res.* **2014**, *5*, 116–123. [[CrossRef](#)]
37. Fornasini, M.L.; Manfrinetti, P.; Gschneidner, K.A. GdMg5: A complex structure with a large cubic cell. *Acta Crystallogr. Sect. C Cryst. Struct. Commun.* **1986**, *42*, 138–141. [[CrossRef](#)]
38. Campos, M.D.R.S.; Blawert, C.; Mendis, C.L.; Mohedano, M.; Zimmermann, T.; Proefrock, D.; Zheludkevich, M.L.; Kainer, K.U. Effect of Heat Treatment on the Corrosion Behavior of Mg-10Gd Alloy in 0.5% NaCl Solution. *Front. Mater.* **2020**, *7*. [[CrossRef](#)]
39. Persson, K. *Materials Data on Mg54Ag17 (SG:71) by Materials Project*; Lawrence Berkeley National Lab. (LBNL): Berkeley, CA, USA, 2020. [[CrossRef](#)]
40. Kraus, T.; Fischerauer, S.F.; Hänzli, A.C.; Uggowitzer, P.J.; Löffler, J.F.; Weinberg, A. Magnesium alloys for temporary implants in osteosynthesis: In vivo studies of their degradation and interaction with bone. *Acta Biomater.* **2012**, *8*, 1230–1238. [[CrossRef](#)]
41. Martynenko, N.; Lukyanova, E.; Serebryany, V.; Prosvirnin, D.; Terentiev, V.; Raab, G.; Dobatkin, S.; Estrin, Y. Effect of equal channel angular pressing on structure, texture, mechanical and in-service properties of a biodegradable magnesium alloy. *Mater. Lett.* **2019**, *238*, 218–221. [[CrossRef](#)]
42. Suh, J.; Victoria-Hernández, J.; Letzig, D.; Golle, R.; Volk, W. Effect of processing route on texture and cold formability of AZ31 Mg alloy sheets processed by ECAP. *Mater. Sci. Eng. A* **2016**, *669*, 159–170. [[CrossRef](#)]
43. Akbaripanah, F.; Fereshteh-Saniee, F.; Mahmudi, R.; Kim, H. Microstructural homogeneity, texture, tensile and shear behavior of AM60 magnesium alloy produced by extrusion and equal channel angular pressing. *Mater. Des.* **2013**, *43*, 31–39. [[CrossRef](#)]

44. Martynenko, N.; Lukyanova, E.A.; Serebryany, V.N.; Gorshenkov, M.; Shchetinin, I.; Raab, G.; Dobatkin, S.V.; Estrin, Y. Increasing strength and ductility of magnesium alloy WE43 by equal-channel angular pressing. *Mater. Sci. Eng. A* **2018**, *712*, 625–629. [[CrossRef](#)]
45. Dobatkin, S.; Galkin, S.; Estrin, Y.; Serebryany, V.; Diez, M.; Martynenko, N.; Lukyanova, E.; Perezhogin, V. Grain refinement, texture, and mechanical properties of a magnesium alloy after radial-shear rolling. *J. Alloy. Compd.* **2019**, *774*, 969–979. [[CrossRef](#)]
46. Nie, J. Precipitation and Hardening in Magnesium Alloys. *Met. Mater. Trans. A* **2012**, *43*, 3891–3939. [[CrossRef](#)]
47. Vostrý, P.; Smola, B.; Stulíková, I.; Von Buch, F.; Mordike, B.L. Microstructure Evolution in Isochronally Heat Treated Mg–Gd Alloys. *Phys. Status Solidi A* **1999**, *175*, 491–500. [[CrossRef](#)]
48. Gao, X.; He, S.; Zeng, X.; Fu, P.; Ding, W.; Nie, J. Microstructure evolution in a Mg–15Gd–0.5Zr (wt.%) alloy during isothermal aging at 250 °C. *Mater. Sci. Eng. A* **2006**, *431*, 322–327. [[CrossRef](#)]
49. Shi, Z.-Z.; Zhang, W.-Z. Enhanced age-hardening response and microstructure study of an Ag-modified Mg–Sn–Zn based alloy. *Philos. Mag. Lett.* **2013**, *93*, 473–480. [[CrossRef](#)]
50. Kim, H.S.; Kim, W.J. Annealing effects on the corrosion resistance of ultrafine-grained pure titanium. *Corr. Sci.* **2014**, *89*, 331–337. [[CrossRef](#)]
51. Song, D.; Ma, A.; Jiang, J.; Lin, P.; Yang, D.; Fan, J. Corrosion behavior of equal-channel-angular-pressed pure magnesium in NaCl aqueous solution. *Corr. Sci.* **2010**, *52*, 481–490. [[CrossRef](#)]
52. Niu, H.-Y.; Deng, K.-K.; Nie, K.-B.; Wang, C.-J.; Liang, W.; Wu, Y. Degradation behavior of Mg–4Zn–2Ni alloy with high strength and high degradation rate. *Mater. Chem. Phys.* **2020**, *249*, 123131. [[CrossRef](#)]
53. Sun, Y.; Wang, R.; Peng, C.; Cai, Z. Microstructure and corrosion behavior of as-extruded Mg–xLi–3Al–2Zn–0.2Zr alloys (x = 5, 8, 11 wt.%). *Corr. Sci.* **2020**, *167*, 108487. [[CrossRef](#)]
54. Birbilis, N.; Ralston, K.; Virtanen, S.; Fraser, H.L.; Davies, C.H.J. Grain character influences on corrosion of ECAPed pure magnesium. *Corr. Eng. Sci. Technol.* **2010**, *45*, 224–230. [[CrossRef](#)]
55. Ralston, K.; Birbilis, N. Effect of Grain Size on Corrosion: A Review. *Corrosion* **2010**, *66*, 075005. [[CrossRef](#)]
56. Dobatkin, S.V.; Lukyanova, E.A.; Martynenko, N.; Anisimova, N.; Kiselevskiy, M.V.; Gorshenkov, M.V.; Yurchenko, N.Y.; I Raab, G.; Yusupov, V.S.; Birbilis, N.; et al. Strength, corrosion resistance, and biocompatibility of ultrafine-grained Mg alloys after different modes of severe plastic deformation. *IOP Conf. Ser. Mater. Sci. Eng.* **2017**, *194*, 12004. [[CrossRef](#)]
57. Zhang, C.; Wu, L.; Liu, H.; Huang, G.; Jiang, B.; Atrons, A.; Pan, F. Microstructure and corrosion behavior of Mg–Sc binary alloys in 3.5 wt.% NaCl solution. *Corr. Sci.* **2020**, *174*, 108831. [[CrossRef](#)]
58. Liu, Y.; Cheng, W.-L.; Liu, Y.-H.; Niu, X.-F.; Wang, H.-X.; Wang, L.-F.; Cui, Z.-Q. Effect of alloyed Ca on the microstructure and corrosion behavior of extruded Mg–Bi–Al-based alloys. *Mater. Charact.* **2020**, *163*, 110292. [[CrossRef](#)]
59. Wang, Y.; Zhang, Y.; Wang, P.; Zhang, D.; Yu, B.; Xu, Z.; Jiang, H. Effect of LPSO phases and aged-precipitations on corrosion behavior of as-forged Mg–6Gd–2Y–1Zn–0.3Zr alloy. *J. Mater. Res. Technol.* **2020**, *9*, 7087–7099. [[CrossRef](#)]
60. Ding, Z.-Y.; Cui, L.-Y.; Zeng, R.-C.; Zhao, Y.-B.; Guan, S.-K.; Xu, D.K.; Lin, C.-G. Exfoliation corrosion of extruded Mg–Li–Ca alloy. *J. Mater. Sci. Technol.* **2018**, *34*, 1550–1557. [[CrossRef](#)]
61. Esmaily, M.; Svensson, J.; Fajardo, S.; Birbilis, N.; Frankel, G.; Virtanen, S.; Arrabal, R.; Thomas, S.; Johansson, L. Fundamentals and advances in magnesium alloy corrosion. *Prog. Mater. Sci.* **2017**, *89*, 92–193. [[CrossRef](#)]
62. Dong, J.-H.; Tan, L.; Ren, Y.; Yang, K. Effect of Microstructure on Corrosion Behavior of Mg–Sr Alloy in Hank’s Solution. *Acta Metall. Sin.* **2018**, *32*, 305–320. [[CrossRef](#)]
63. Zhang, Y.; Li, J.; Lai, H.; Xu, Y. Effect of Homogenization on Microstructure Characteristics, Corrosion and Biocompatibility of Mg–Zn–Mn–xCa Alloys. *Materials* **2018**, *11*, 227. [[CrossRef](#)] [[PubMed](#)]

